

# Evaluation of Ultra-High Temperature Ceramics for Aeropropulsion Use

Stanley R. Levine\*, Elizabeth J. Opila, Michael C. Halbig, James D. Kiser,

Mrityunjay Singh, and Jonathan A. Salem

NASA Glenn Research Center

Cleveland, OH 44135

## ***Abstract***

*Among the ultra-high temperature ceramics (UHTC) are a group of materials consisting of zirconium diboride or hafnium diboride plus silicon carbide, and in some instances, carbon. These materials offer a good combination of properties that make them candidates for airframe leading edges on sharp-bodied reentry vehicles. These UHTC perform well in the environment for such applications, i.e. air at low pressure. The purpose of this study was to examine three of these materials under conditions more representative of a propulsion environment, i.e. higher oxygen partial pressure and total pressure. Results of strength and fracture toughness measurements, furnace oxidation, and high velocity thermal shock exposures are presented for  $ZrB_2$  plus 20 volume % SiC,  $ZrB_2$  plus 14 volume % SiC plus 30 volume % C, and SCS-9a SiC fiber reinforced  $ZrB_2$*

*plus 20 volume % SiC. The poor oxidation resistance of UHTCs is the predominant factor limiting their applicability to propulsion applications.*

*Keywords:* borides, composites, corrosion, thermal shock resistance, engine components.

\* To whom correspondence should be addressed.

## **1 Introduction**

The high melting points of refractory metal diborides coupled with their ability to form refractory oxide scales give these materials the capability to withstand temperatures in the 1900 to 2500°C range. These ultra-high temperature ceramics were developed in the 1960's <sup>1</sup>. Fenter <sup>2</sup> provides a comprehensive review of the work accomplished in the 1960's and early 1970's. Additions of silicon carbide are used to enhance oxidation resistance and limit diboride grain growth. Carbon is also sometimes used as an additive to enhance thermal stress resistance. These materials offer a good combination of properties that make them candidates for airframe leading edges on sharp-bodied reentry vehicles <sup>3</sup>. UHTC perform well in the environment for such applications, i.e. air at low pressure. Some interest has also been shown in these materials for single use propulsion applications <sup>4</sup>. The purpose of this study was to examine three of these materials under conditions representative of propulsion environments, i.e. higher oxygen partial pressure and total pressure. Relatively long, multiple exposure cycles are emphasized. Results of strength and fracture toughness measurements, furnace oxidation, and high velocity thermal shock exposures are presented for ZrB<sub>2</sub> plus 20 volume % SiC (abbreviated as

ZS),  $\text{ZrB}_2$  plus 14 volume % SiC plus 30 volume % C (ZSC), and SCS-9a SiC fiber reinforced  $\text{ZrB}_2$  plus 20 volume % SiC (ZSS).  $\text{HfB}_2$  based compositions were not included in the study due to their high cost.

## 2 Materials and Experimental Procedures

### 2.1 Materials

The materials investigated are listed in Table 1. They were fabricated by uniaxial hot pressing by Materials and Machines, Inc., Tucson, Arizona. The powder constituents were obtained from H.C. Starck ( $\text{ZrB}_2$  and SiC), Elkem (silicon), Asbury Graphite Mills (carbon), and the SiC fibers from Textron Specialty Materials (SCS-9a fibers).

The ZS and ZSC billet dimensions were nominally 2.8 cm high by 10 cm diameter. ZS had an average density of  $5.57 \text{ gm/cm}^3$  (100% of theoretical density), and the ZSC had billet densities of 4.47 and  $4.54 \text{ gm/cm}^3$  (98.2 and 99.9 % of theoretical density, respectively).

Specimens were mounted in epoxy and polished, then examined via field emission scanning electron microscopy (FESEM) with a Hitachi S-4700 Field Emission SEM with XEDS (X-ray energy dispersive spectroscopy) capability. A representative ZS material microstructure is shown in Figure 1. The  $\text{ZrB}_2$  grains (gray phase) are equiaxed, with the majority of the grains ranging from 6 to  $12 \text{ }\mu\text{m}$  in width. The SiC (dark phase) grains appear to be elongated/tabular (approximately 1.5 to  $3 \text{ }\mu\text{m}$  thick by 3 to  $11 \text{ }\mu\text{m}$  wide/long). ZS was virtually pore-free, and individual large SiC or  $\text{ZrB}_2$  particles (width  $\geq 20 \text{ }\mu\text{m}$ ) that could act as strength-reducing flaws were not observed in the polished

cross sections. Significant grain-pullout occurred during the polishing of the ZSC material as shown in Figure 2a. This is attributed to the presence of the 30 volume % C, which apparently led to weaker bonding within this UHTC. For comparison, a ZSC fracture surface is shown in Figure 2b to confirm that the material is close to fully dense.

The composite panel was prepared by the filament winding and slurry deposition technique followed by hot pressing in a graphite die. The final composite panel was 15.1 by 15.1 by 0.53 cm with a density of 3.47 gm/cm<sup>3</sup>, while the theoretical density is 4.60 gm/cm<sup>3</sup> for 35 volume % fiber loading. ZSS composite specimens were mounted in epoxy and polished, then examined via optical microscopy and FESEM. A representative ZSS composite microstructure is shown in Figure 3a. The SCS-9a fibers have a diameter of about 80  $\mu$ m including the dual layer coating. It appears that the coating on the surface of the SCS-9a fibers remained intact during the hot pressing process. The fiber volume fraction within the multilayer plies was at the target 0.30. However thick matrix layers between plies reduced the overall fiber volume fraction to 0.20 to 0.25. Significant amounts of porosity can be seen in the matrix (Figure 3b). Based on the density of the billet and a rule of mixtures calculation, the matrix material is approximately 70 % dense. Longitudinal sections revealed regularly spaced matrix cracks (400 to 800  $\mu$ m apart) oriented perpendicular to the fibers. These cracks are due to the matrix thermal expansion coefficient being greater than that of the fiber and thus leading to cracking upon cooling from the processing temperature, as is observed in other composites such as C/SiC.

## **2.2 Procedures**

### **2.2.1 Mechanical properties**

Flexural Strength—Test bars (3 by 4 by 50 mm, with four long edges beveled) were machined from each billet of monolithic UHTC material. Test bars (5 by 6 by 50 mm with no beveling of edges) were also machined from the ZSS billet. Specimens were tested in four-point flexure (20/40 mm inner/outer spans, silicon carbide fixture, 0.5 mm/min. loading rate) in air at 25, 1127, and 1327°C. The load was applied to the samples after the test temperature was achieved. Four monolithic and two composite specimens were tested per test condition. Fractography was performed on various tested monolithic specimens, to assess the nature of the critical flaws.

Creep—Monolithic (ZS and ZSC) specimens were tested in four-point flexure (20/40 mm inner/outer spans, silicon carbide fixture) in air at 1127 and 1327°C. Upon reaching the test temperature, ZS and ZSC samples were loaded to half the average measured strength of the material at the test temperature. Thus, ZS samples were loaded at 250 MPa and 180 MPa at 1127 and 1327°C, respectively. ZSC samples were loaded at 100 MPa and 90 MPa at 1127 and 1327°C, respectively. Samples were held for 5 hours. The steady state creep rate was determined. Two specimens were tested per test condition.

Fracture Toughness - Single edge pre-cracked beam testing in accordance with ASTM C 1421<sup>5</sup> was used to determine the fracture toughness of the ZS and ZSC materials. Six tests were conducted per material.

### 2.2.2 Furnace Oxidation

Sample coupons were 2.54 by 1.27 by 0.32 cm. Coupons were ultrasonically cleaned successively in detergent, de-ionized water, acetone and alcohol prior to exposure. Initial sample weights (to an accuracy of 0.00005g) and dimensions (to an accuracy of 0.001 cm) were recorded. Three samples were loaded into a slotted ZrO<sub>2</sub> refractory brick. Samples were exposed to ten-minute oxidation cycles in stagnant air at 1327°C in a box furnace with molybdenum disilicide heating elements (CM, Inc. Rapid Temp Furnace, Bloomfield NJ). One sample was removed after one cycle, five cycles and ten cycles. A maximum exposure time of 100 minutes was thus achieved. Similar exposures were conducted at 1627 and 1927°C using a bottom-loading furnace with zirconia heating elements (DelTech, Inc., Denver, CO). Weight change was measured, where possible. Some of the samples stuck to the sample holder during oxidation due to extensive glass formation. X-Ray Diffraction (XRD) was used to identify oxide phases present after exposure. After surface microstructural analysis by SEM and XEDS, samples were cross-sectioned and polished to 1µm diamond in non-aqueous polishing media. Water was avoided to preserve any boron that might be present as an oxidation product. The amount of surface recession was determined from the difference between the initial thickness and the thickness of unreacted material that was measured in low magnification SEM micrographs of sample cross-sections. Thickness measurements obtained from micrographs were corrected based on a magnification reference standard.

### 2.2.3 Thermal Shock

Thermal shock tests were run by placing 1.27 by 0.32 by 8.31 cm specimens of ZS or ZSC specimens in a copper block holder in front of a hydrogen-oxygen combustor and nozzle assembly operating at a chamber pressure of 1.75 MPa. For comparison purposes, a silicon nitride specimen with similar test section dimensions except for a width of 1.02 cm in the gage section was tested. The flame impinged along the length of the specimen on the thin edge (thickness) dimension. Initial 5 s runs were made at an oxygen to hydrogen (O:H) mixture ratio of 1.7 to achieve a target gas temperature of 1327°C. Two runs were made at an O:H mixture ratio of 2.3 to achieve a target gas temperature of 1627°C. The flame was turned from off to full on and from full on to off. Then the specimens were exposed to an ambient temperature nitrogen purge that impinged on the cooling specimen. Due to mixing problems in the combustor, the target temperatures were not achieved. Hot streaks to temperatures much higher than the target temperature were present near the periphery of the flame, and the center of the specimen ran cooler as a result of oxygen gas flow through a central igniter tube. In the earlier tests the specimens were clamped loosely in the holder at one end. A compliant high temperature fabric was used to clamp the specimen ends in the later tests. Visual observations, photographs, some XRD analysis of the surface, and metallography documented test results.

### 3 Results

#### 3.1 Mechanical properties

Flexural strength - Limited flexural testing in fast fracture was performed for the ZS and ZSC materials, and results are presented in Tables 2 and 3, respectively. The flexural strength of ZS is comparable to a reported literature value of 408 MPa at room temperature <sup>6</sup>. The large scatter in our limited number of tests is indicative of material variability due to poor process control. The ZSC material has a lower average strength at room temperature, and shows diminished strength at higher temperature. The 30 volume % C is the probable cause of the reduced strength. The grain pullout observed during polishing of the samples indicates weaker bonding within the material.

Fractography was performed to assess the nature of the critical flaws in various monolithic specimens tested at room temperature. The fracture origins were usually difficult to locate. Large clusters of relatively coarse  $\text{ZrB}_2$  grains surrounding groups or clusters of large SiC grains were observed within the fracture mirror and fracture was often attributed to these features. The former often took on a more or less spherical shape indicating the possibility of spherical agglomerates that had not separated from the surrounding matrix during sintering. The SiC clusters were in a chain-like series of grains within the  $\text{ZrB}_2$  matrix indicating the possibility of partially broken down agglomerates. Because of the large scatter in the data, no trends with increasing temperature could be discerned.



The composite samples showed through thickness cracks during testing, but did not separate into 2 separate pieces due to crack bridging by the fibers. Delaminations were also observed. Results are summarized in Table 4.

Creep – Minimal deformation was observed for the ZS and ZSC materials during the 5 h creep tests. Very low steady state creep rates were observed for the ZS material (Table 2). Rates of  $2.6 \times 10^{-10} \text{ sec}^{-1}$  and  $2.5 \times 10^{-9} \text{ sec}^{-1}$  at 250 MPa/1127°C and 180 MPa/1327°C, respectively, were observed. Total strain (mm/mm) under those conditions was as follows:  $4.8 \times 10^{-5}$  and  $1.5 \times 10^{-4}$ , respectively. In spite of the presence of 30 v/o C, and the potential for oxidation of that C, low ZSC creep rates were observed (Table 3). Rates of  $1.4 \times 10^{-9} \text{ sec}^{-1}$  and  $1.6 \times 10^{-8} \text{ sec}^{-1}$  at 100 MPa/1127°C and 90 MPa/1327°C, respectively, were observed. Total strains (mm/mm) under these conditions were  $5.6 \times 10^{-5}$  and  $5.4 \times 10^{-4}$ , respectively.

Fracture toughness – The six valid tests completed on the ZS material gave a fracture toughness of  $K_{Ipb} = 4.45 \pm 0.32 \text{ MPa}\sqrt{\text{m}}$ . Five valid test results on the ZSC material indicated a fracture toughness of  $K_{Ipb} = 4.82 \pm 0.15 \text{ MPa}\sqrt{\text{m}}$ . All test specimens exhibited stable crack extension as monitored with back face strain gages or the actuator stroke. One difficulty encountered in the ZSC testing was measurement of the crack length: the test specimens tended to absorb the dye penetrant use to mark the crack fronts. Thus the crack length could be measured only if the pre-crack plane and the fast fracture plane were not completely coplanar, thereby demarking the precrack front. This was the case in five of six attempted tests with ZSC.

### **3.2 Furnace Oxidation**

Macrographs of the ZS samples after oxidation are shown in Figure 4. Oxide formation is visible on the samples tested at 1327°C. Extensive glass formation was observed on samples exposed at 1627°C. Samples oxidized at 1927°C formed an orange oxide after one 10-minute cycle. With increasing exposure time, the oxide scale became grayer. At this exposure temperature, swelling of the samples occurred with the thickness of the specimens increasing by up to 80% after ten 10-minute cycles. XRD analyses show the surface oxidation product is largely monoclinic  $\text{ZrO}_2$  under all conditions. An SEM photomicrograph of the surface of ZS after oxidation for one 10-minute cycle at 1327°C is shown in Figure 5. The large white crystals on the surface are  $\text{SiO}_2$  and the irregularly shaped material in the background is a mixture of  $\text{SiC}$ ,  $\text{ZrO}_2$  and  $\text{SiO}_2$ .

Figure 6 shows macrographs of the ZS sample cross-sections after oxidation. Oxide scales are visible to the unaided eye beginning with exposures at 1627°C. The sample exposed at 1927°C for ten 10-minute cycles is almost completely consumed.

SEM and XEDS results for ZS sample cross-sections are shown in Figures 7 through 9. SEM and XEDS results were obtained at 6kV where sensitivity to boron is high. After exposure at 1327°C for ten 10-minute cycles, the oxide scale was about 30  $\mu\text{m}$  thick and composed of  $\text{ZrO}_2$  with  $\text{SiC}$  particles embedded in the scale as shown in Figure 7. XEDS analysis of the  $\text{ZrO}_2$  scale in this and all subsequent samples showed some boron content. Figure 8 shows a ZS sample cross-section after exposure at 1627°C for ten 10-minute cycles as well as the results of an XEDS line scan. The oxide scale was about 150  $\mu\text{m}$  thick. Beginning from the surface, the scale was composed of amorphous  $\text{SiO}_2$  followed by a layer consisting primarily of  $\text{ZrO}_2$  in a continuous silica-rich glassy phase. No boron

was detected in the glassy phase. A discrete  $\text{ZrO}_2/\text{ZrB}_2$  boundary was followed by a SiC depleted region of  $\text{ZrB}_2$  of about another 100  $\mu\text{m}$  thickness. This SiC depletion layer was observed in previous work, both the work at high temperatures and high oxygen partial pressures<sup>1</sup> as well as in exposures at lower temperatures, but only in reduced oxygen partial pressures<sup>6</sup>. This SiC depletion was attributed to active oxidation of the SiC to form  $\text{SiO(g)}$ <sup>6</sup>. Figure 9 shows the ZS sample cross-section after exposure at 1927°C for ten 10-minute cycles. Here, the oxide scale was several mm thick. The scale was composed of large  $\text{ZrO}_2$  grains in a silica-rich glassy phase. No SiC depletion layer was observed.

Figure 10 shows the surface appearance of the three materials examined in this study after oxidation exposures of 1, 5, and 10 ten-minute cycles at 1327°C. The most compact and homogeneous scale is formed on the ZS formulation. This is supported by the weight change data for ZS and ZSC shown in Figure 11. Weight increases are due to the formation of  $\text{ZrO}_2$ . ZSC oxidizes more rapidly than ZS due to the presence of porosity resulting from the oxidation of C and scale disruption due to CO formation. The weight loss for the SCS-9a fiber reinforced material is in large measure due to the loss of the ~ 10  $\mu\text{m}$  carbon cores of the fibers. Figure 12 illustrates the near parabolic oxidation kinetics exhibited by ZS and ZSC at 1327°C.

Figure 13 shows the surface appearance of the ZS, ZSC, and ZSS materials after oxidation exposures of 1, 5, and 10 ten-minute cycles at 1627°C. The most compact and homogeneous scale is again formed on the ZS formulation. Weight change data in Figure 14 shows near parabolic behavior for ZS, deviation from parabolic behavior for ZSC due

to scale spallation, and a recovery from the weight loss of fiber carbon cores in ZSS as a result of the rapid kinetics of oxidation of the porous matrix to form  $\text{ZrO}_2$ .

Figure 15 shows the surface appearance of the three materials examined in this study after oxidation exposures of 1, 5, and 10 ten-minute cycles at  $1927^\circ\text{C}$ . Extensive distress in the form of cracks, nodules, and spallation is evident in the scales on all three materials. ZSS was severely bloated as a result of oxidation. The weight change plots in Figure 16 are indicative of this distress with parabolic behavior no longer evident in ZS, and large weight losses evident at 5 and 10 cycles in ZSC and ZSS.

### 3.3 Thermal Shock

Bull et al <sup>3</sup> used the following thermal shock parameter (TSP) for ZS:

$$\text{TSP} = \frac{24k\sigma_f(1-\mu^2)}{\alpha E} = 1.8 \times 10^5 \text{ W/m}$$

Here  $k$  is thermal conductivity,  $\sigma_f$  is flexural strength,  $\mu$  is Poisson's ratio,  $\alpha$  is coefficient of thermal expansion, and  $E$  is elastic modulus. The TSP value for the AS-800 silicon nitride reference material used in our study is  $8.6 \times 10^5$  based on reported property values <sup>7</sup>. This is indicative of better thermal shock resistance from AS-800 compared to ZS.

Results of thermal shock tests are summarized in Figure 17 and Table 5. One of two ZS samples survived 5 s exposures at O:H of 1.7, as did a ZSC and the AS-800 sample. Other tests of AS-800 resulted in survival of hundreds of cycles (A.E. Eckel, private communication). The AS-800 sample appeared to oxidize to a lesser extent than the

UHTCs. ZSC oxidized to a greater extent than ZS. Longer duration exposures at O:H of 1.7 resulted in more extensive oxidation and, in some cases, erosion. In most cases the samples fractured. At the higher O:H of 2.3, samples of each UHTC material were severely eroded after 180 s of exposure.

As noted after the furnace oxidation exposures, XRD analysis of the heat affected zones of the ZS and ZSC thermal shock specimens show the oxidation product to be mainly monoclinic zirconia. Some SiC was also detected on specimen F6925 exposed for 210 s at the lower O:H ratio,. This is in agreement with the furnace oxidation results at 1327°C. In some cases the cubic zirconia phase was also detected. For short exposures where the scales were thin, the underlying ZrB<sub>2</sub> phase was detected.

Based on the performance of the UHTCs in this test, thermal shock appears to be a concern in high heat flux aeroconvective environments such as might be encountered in propulsion applications.

#### **4 Discussion**

The three UHTCs examined in this study were not exposed under conditions for which they appear to be best suited, but rather for application in an aeropropulsion environment where oxygen and, if hydrogen containing fuel is being combusted, water vapor partial pressures are much higher than in reentry to the earth's atmosphere from space. The capability of these materials for propulsion applications must be compared to mature, available, and commercially used ceramics such as silicon nitride, e.g. AS-800, to put things in proper perspective.

In terms of mechanical properties, the UHTCs fall short in terms of strength and fracture toughness. At about 1300°C the creep resistance of ZS as measured here (in flexure) appears to be superior to the creep resistance reported for AS-800 (in tension) <sup>7</sup>. However, the stress rupture life for Si<sub>3</sub>N<sub>4</sub> under stress and temperature conditions similar to those used in this study is measured in hundreds of hours <sup>7</sup>. ZS could not achieve such lives due to the oxidation issue. At their current state of early development it appears that reproducibility of mechanical properties, and thus material reliability is an issue for UHTCs whereas the considerable efforts put into process development for silicon nitride over the past 30 years have tightened material property scatter. <sup>e.g. 7</sup>

In terms of oxidation resistance, acceptable amounts of material recession in one hour to thousands of hours, depending on the specific propulsion application, are on the order of 100 to 300 micrometers. This converts to an acceptable range of parabolic recession rate constants,  $k_p''$ , of approximately less than or equal to  $10^{-1}$  to  $10^{-2}$  mm<sup>2</sup>/h for a one hour application. For a 100 hour application an acceptable range of  $k_p''$  would be less than or equal to the above values divided by 100. Measured parabolic recession rate constants in mm<sup>2</sup>/h for the more oxidation resistant ZS material were  $4.7 \times 10^{-3}$  at 1327°C,  $7.8 \times 10^{-2}$  at 1627 °C, and 1.3 at 1927 °C <sup>8</sup>. Thus recession rate constants for ZS are acceptable at 1327 °C for a one-hour application, but here silicon nitride is a superior material. At 1627 °C ZS oxidation is marginal for a one-hour application. But dimensional growth would be an issue. In a 100-hour application ZS cannot be considered at any temperature. Prospects for the orders of magnitude improvement in oxidation resistance required for UHTC propulsion applications are not good. Zirconia rich scales (or for that matter hafnia rich scales in the case of hafnium diboride based materials) provide poor

oxidation protection. This is due to the rapid oxygen transport and the disruptive phase transformation that are characteristics of zirconia.

Resistance to water vapor is another issue of concern for materials in propulsion applications. It is known that  $\text{SiO}_2$  formers, e.g. SiC, lose silicon as  $\text{Si(OH)}_x(\text{g})$  species at high temperature in the presence of water vapor<sup>9</sup>. This problem is also a major issue for silicon nitride<sup>10</sup>. In addition  $\text{B}_2\text{O}_3$  reacts with water vapor<sup>11</sup> to form volatile species such as  $\text{HBO}_4$ . Thus one would expect water vapor to aggressively attack the UHTCs. Indeed this is reported to be the case (Q.N. Nguyen and R.C. Robinson, private communication).

Our cursory examination of thermal shock, both from a theoretical and experimental viewpoint, indicated that the ZS and ZSC UHTCs have less thermal shock resistance relative to AS-800 silicon nitride.

## 5 Conclusions

Based on the results of this limited study, the three examined UHTCs are not ready to be considered as aeropropulsion materials for any applications longer than a few minutes. Current materials suffer from aggressive oxidation and moisture attack. Processing does not appear to be under control as evidenced by large scatter in mechanical property data. This property scatter combined with low fracture toughness leads to poor resistance to thermal shock. The key to raising their potential for any application is to improve process and thus material reproducibility. For long-term propulsion applications major improvements in environmental durability are needed. Given the inherent rapid oxygen

transport rates and disruptive phase transformation characteristics of zirconia (and hafnia), such orders of magnitude improvements for propulsion applications are unlikely.

### Acknowledgement

This work was inspired by the NASA Administrator, Mr. Daniel Goldin.

### References

1. Clougherty, E.V., Poher, R.L. & Kaufman, L., Synthesis of oxidation resistant metal diboride composites. *Trans. Met. Soc. AIME*, 1968, **242**, 1077-1082.
2. Fenter, J.R., Refractory diborides as engineering materials. *SAMPE Quarterly*, 1971, **2**, 1-15.
3. Bull, J.D., Rasky, D.J. & Karika, C.C., Stability characterization of diboride composites under high velocity atmospheric flight conditions. *24<sup>th</sup> International SAMPE Technical Conference*, 1992, pp. T1092- T1106.
4. Opeka, M.M., Talmy, I.G., Wuchina, E.J., Zaykoski, J.A. & Causey, S.J., Mechanical, thermal, and oxidation properties of refractory hafnium and zirconium compounds. *J. Eur. Cer. Soc.*, 1999, **19**, 2405-2414.
5. ASTM C 1421-99, Standard test method for the determination of fracture toughness of advanced ceramics at ambient temperatures, *Annual Book of ASTM Standards, V. 15.01*, American Society for Testing and Materials, West Conshohocken, Pennsylvania (1999).



6. Tripp, W.C., Davis, H.H. & Graham, H.C., Effect of an SiC addition on the oxidation of ZrB<sub>2</sub>. *Cer. Bull.*, 1973, **52**, 612-616.
7. Pollinger, J.P., Status of silicon nitride component fabrication processes, material properties, and applications. ASME Turbo Expo 97, Paper 97-GT-321, The American Society of Mechanical Engineers, New York, 1997.
8. Opila E.J. & Halbig, M.C., Oxidation of ZrB<sub>2</sub>-based ultra-high temperature ceramics. *Ceramic Engineering and Science Proceedings*, 2001, **XX**, pp.
9. Robinson R.C. & Smialek, J.L., SiC recession caused by SiO<sub>2</sub> scale volatility under combustion conditions: I, experimental results and empirical model. *J. Amer. Cer. Soc.*, 1999, **82**, 1817-25.
10. Jacobson, N.S., Opila, E.J., Fox, D.S., & Smialek, J.L., Oxidation and corrosion of silicon-based ceramics and composites. *High Temperature Corrosion And Protection Of Materials 4, Pts 1 And 2*, **251-2**, 817-831 (1997).
11. Jacobson, N.S., Farmer, S., Moore, A., & Sayir, H., High-temperature oxidation of boron nitride: I, monolithic boron nitride. *J. Amer. Cer. Soc.*, 1999, **82**, 393-491.

## List of Figures

- Figure 1. Microstructure of  $\text{ZrB}_2$  plus 20 v/o SiC ultra-high temperature ceramic.
- Figure 2. Microstructure of  $\text{ZrB}_2$  plus 14 v/o SiC plus 30 v/o C ultra-high temperature ceramic (a) polished section and (b) fracture surface.
- Figure 3. Microstructure of polished sections of  $\text{ZrB}_2$  plus 20 v/o SiC plus SCS-9a fibers composite showing (a) representative fiber distribution and (b) matrix porosity.
- Figure 4. ZS UHTC oxidized in air for 10-minute cycles.
- Figure 5. SEM micrograph of ZS after oxidation in air for 10 minutes at  $1327^\circ\text{C}$ .
- Figure 6. Cross-sections of ZS oxidized in air for 10-minute cycles.
- Figure 7. SEM micrograph and XEDS analysis of phases in ZS after oxidation in air at  $1327^\circ\text{C}$  for ten 10-minute cycles.
- Figure 8. SEM micrograph and XEDS line scan of ZS after oxidation in air at  $1627^\circ\text{C}$  for ten 10-minute cycles.
- Figure 9. SEM micrograph and the results of XEDS analysis for ZS after oxidation in air at  $1927^\circ\text{C}$  for ten 10-minute cycles.
- Figure 10. Comparison of UHTC oxidized in air at  $1327^\circ\text{C}$  for 10-minute cycles.
- Figure 11. Oxidation behavior of UHTC at  $1327^\circ\text{C}$  in air.
- Figure 12. Parabolic oxidation behavior displayed by ZS and ZSC at  $1327^\circ\text{C}$  in air.
- Figure 13. Comparison of UHTC oxidized in air at  $1627^\circ\text{C}$  for 10 minute cycles.

- Figure 14      Oxidation behavior of UHTC at 1627°C in air.
- Figure 15      Comparison of the oxidation behavior of UHTC oxidized in air at 1927°C  
for 10-minute cycles.
- Figure 16      Oxidation behavior of UHTC at 1927°C in air.
- Figure 17      Photographs of specimens tested in thermal shock.

Table 1. Materials

Material Type	Fabrication	Composition ( <i>Abbreviated designation</i> )
Monolithic materials	Hot pressed billets ~ 10 cm diameter by 2.8 cm high	ZrB <sub>2</sub> plus 20 v/o SiC, (ZS)
		ZrB <sub>2</sub> plus 14 v/o SiC plus 30 v/o C, (ZSC)
Composite	Hot pressed plate with uniaxial fiber reinforcement	35 v/o SCS-9a fibers plus ZrB <sub>2</sub> plus 20 v/o SiC, (ZSS)

Table 2. Mechanical Properties of ZS Ultra-High Temperature Ceramic

Four-Point Flexure Tests			
Test Temperature	Number Of Tests	Average Flexural Strength ( $\sigma$ ), MPa	Range( $\sigma$ ), MPa
25 °C	4	391	293 - 456
1127°C	4	497	293 - 666
1327°C	4	356	227 – 500
Flexural Creep Tests (Four-Point Loading)			
Test Temperature	Number Of Tests	Stress Applied ( $\sigma_A$ ), MPa	Steady State Creep Rate, s <sup>-1</sup>
1127°C	2	250	$2.6 \times 10^{-10}$
1327°C	2	180	$2.5 \times 10^{-9}$
Fracture Toughness (Single Edge Precracked Beam (SEPB))			
Test Temperature	Number Of Tests	Average Fracture Toughness, MPa*m <sup>1/2</sup>	S.D., MPa*m <sup>1/2</sup>
25 °C	6	4.45	$\pm 0.32$

Table 3. Mechanical Properties of ZSC Ultra-High Temperature Ceramic

Four-Point Flexure Tests			
Test Temperature	Number Of Tests	Average Flexural Strength ( $\sigma$ ), MPa	Range( $\sigma$ ), MPa
25 °C	4	286	270-301
1127°C	4	206	189-233
1327°C	4	183	172-205
Flexural Creep Tests (Four-Point Loading)			
Test Temperature	Number Of Tests	Stress Applied ( $\sigma_A$ ), MPa	Steady State Creep Rate, s <sup>-1</sup>
1127°C	2	100	$1.4 \times 10^{-9}$
1327°C	2	90	$1.6 \times 10^{-8}$
Fracture Toughness (Single Edge Precracked Beam (SEPB))			
Test Temperature	Number Of Tests	Average Fracture Toughness, MPa*m <sup>1/2</sup>	S.D., MPa*m <sup>1/2</sup>
25 °C	5	4.82	$\pm 0.15$

Table 4. Mechanical Properties of ZSS Ultra-High Temperature Ceramic

Four-Point Flexure Tests			
Test Temperature	Number Of Tests	Average Flexural Strength ( $\sigma$ ), MPa	Elastic modulus, MPa
25 °C	2	130	34.5
1127°C	2	101	33
1327°C	2	84.5	31

Table 5. Thermal Shock of UHTCs

Specimen Number	Material	O/F	Target Temperature, °C	Exposure Time, s	Observations
N1382	Si3N4(AS-800)	1.7	1327	5	survived, minimal silica flow along surface
F6923	ZS	1.7	1327	5	cracked during cool down
F6924	ZS	1.7	1327	5	survived*, minimal oxidation mostly at hot spot
F6925	ZS	1.7	1327	210	cracked*, significant oxidation on surface
F6926	ZS	2.3	1627	180	significant material loss, half of sample broke away*
F6913	ZSC	1.7	1327	5	survived*, minimal oxidation on surface
F6914	ZSC	1.7	1327	75	survived*, significant oxidation on surface
F6915	ZSC	2.3	1627	180	cracked, significant material loss due to spallation*

\* A special high temperature fabric used at the tabs to provide a compliant layer between the sample holder and the specimens.



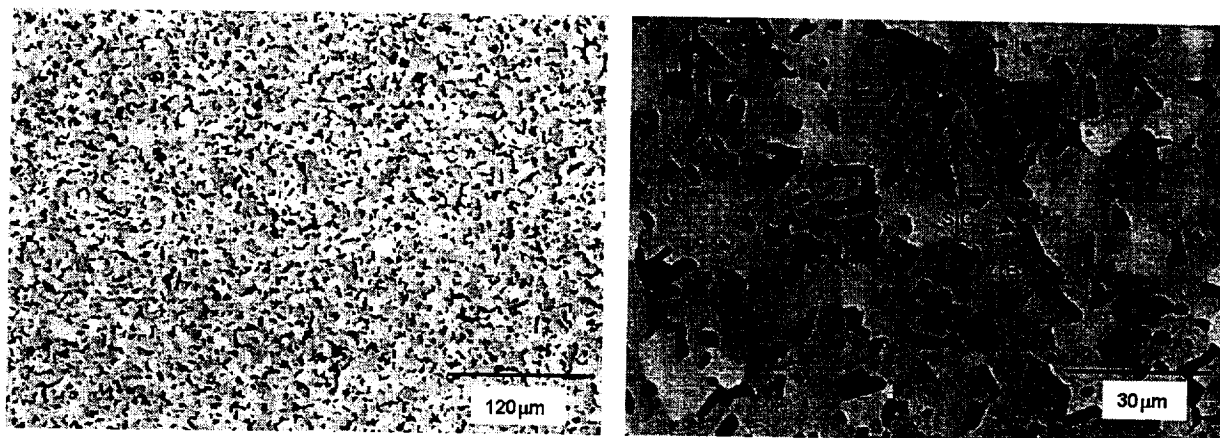


Figure 1. Microstructure of  $\text{ZrB}_2$  plus 20 v/o SiC ultra-high temperature ceramic.

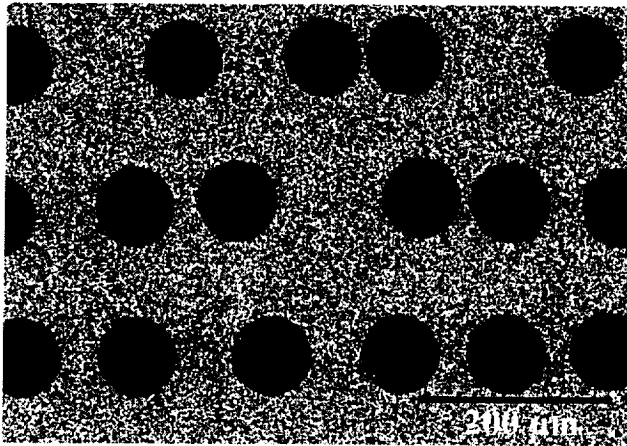


(a)

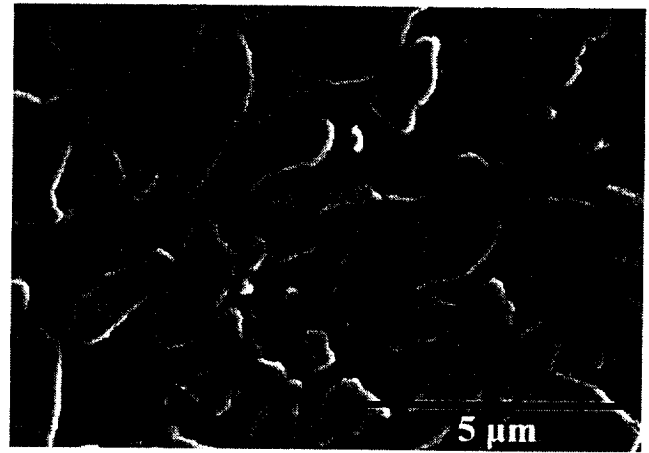


(b)

Figure 2. Microstructure of ZrB<sub>2</sub> plus 14 v/o SiC plus 30 v/o C ultra-high temperature ceramic (a) polished section and (b) fracture surface.



(a)



(b)

Figure 3. Microstructure of polished sections of  $\text{ZrB}_2$  plus 20 v/o SiC plus SCS-9a fibers composite showing (a) representative fiber distribution and (b) matrix porosity.

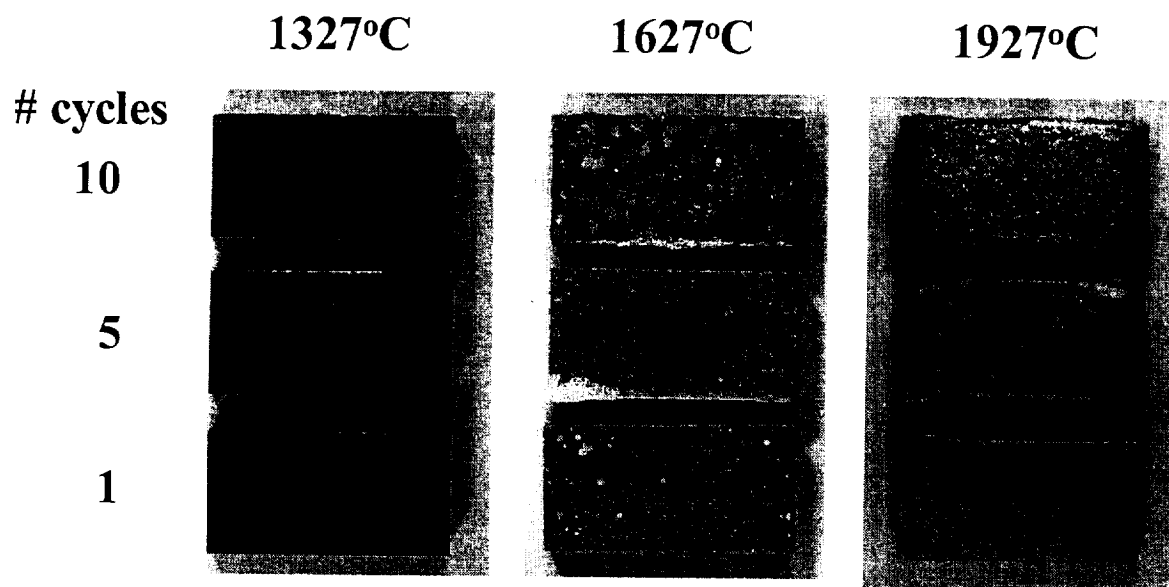


Figure 4. ZS UHTC oxidized in air for 10 minute cycles.

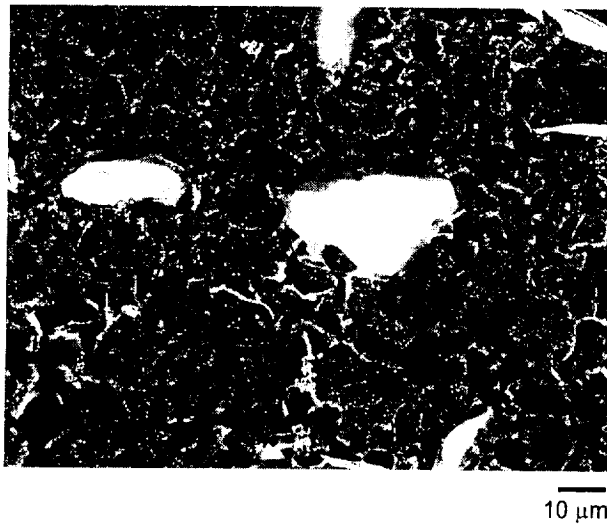


Figure 5. SEM micrograph of ZS after oxidation in air for 10 min at 1327°C.

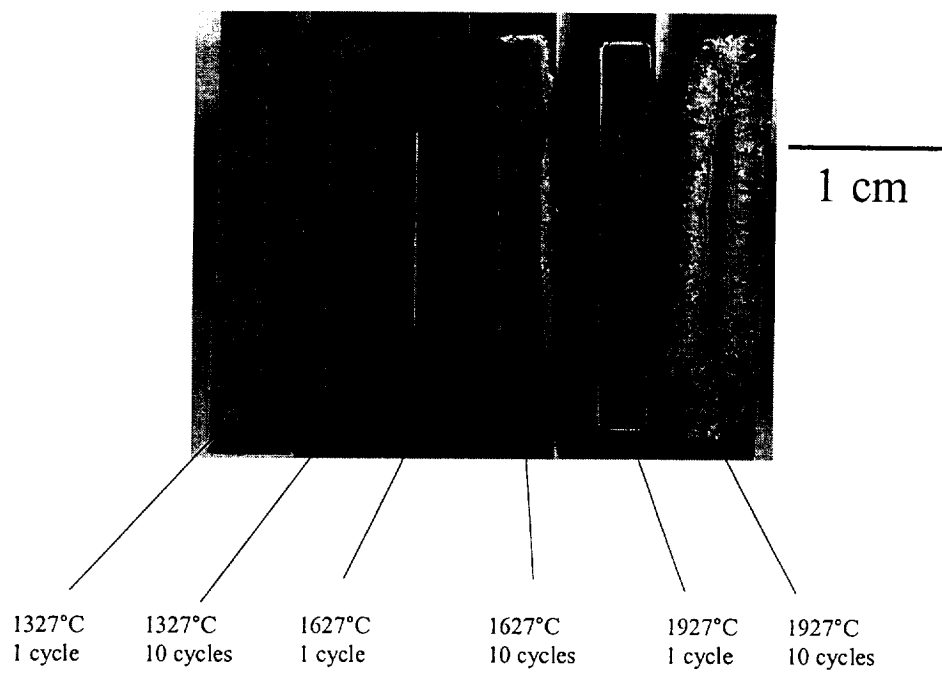


Figure 6. Cross-sections of ZS oxidized in air for 10 min cycles.

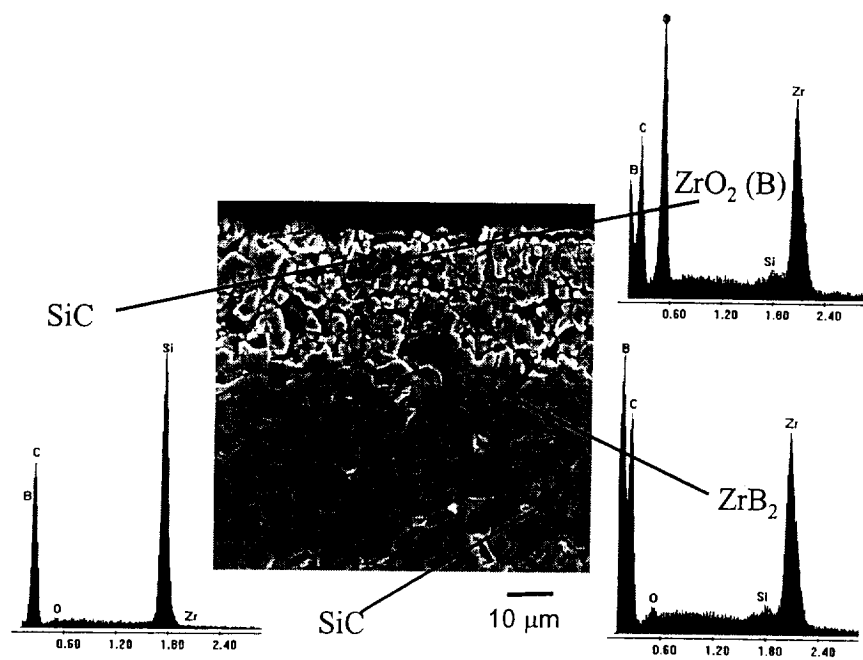


Figure 7. SEM micrograph and EDS analysis of phases in ZS after oxidation in air at 1327°C for ten 10 min cycles.

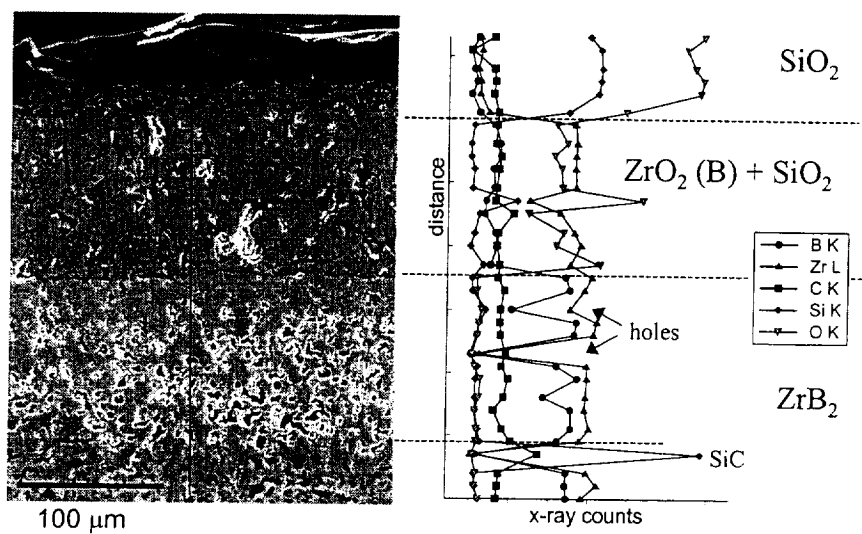


Figure 8. SEM micrograph and EDS line scan of ZS after oxidation in air at 1627°C for ten 10 min cycles.



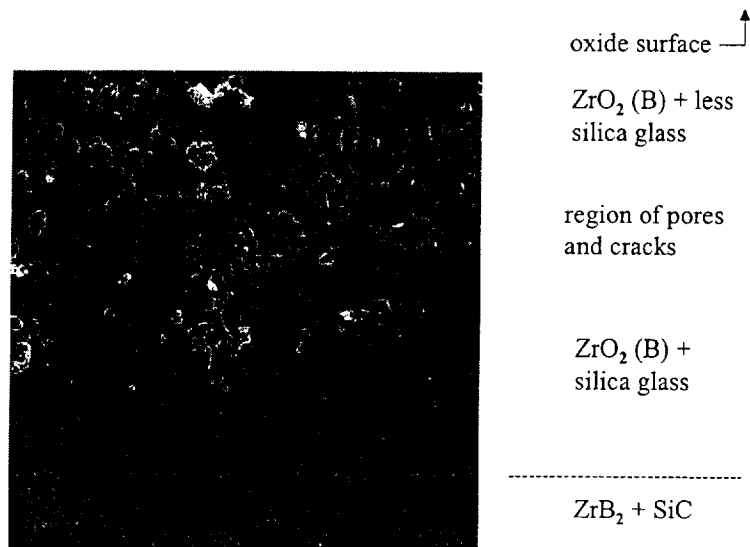


Figure9. SEM micrograph and the results of EDS analysis for ZS after oxidation in air at 1927°C for ten 10 min cycles.

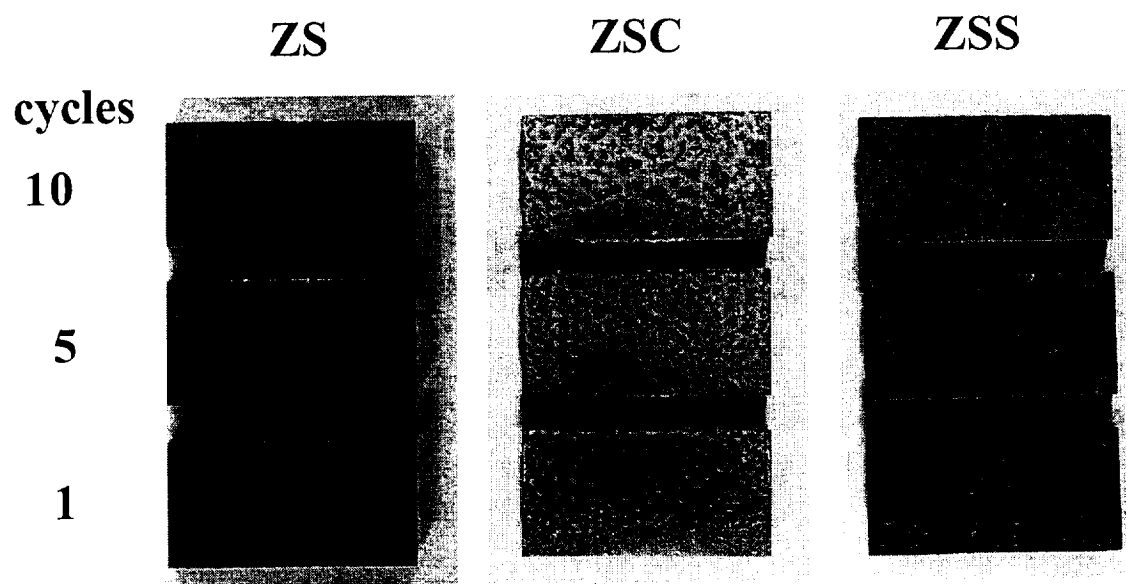


Figure 10. Comparison of UHTC oxidized in air at 1327°C for 10 minute cycles.

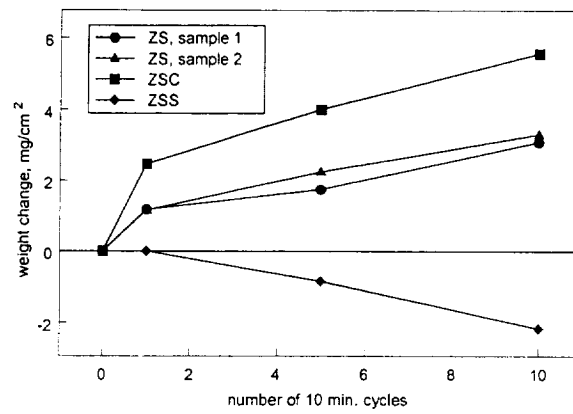


Figure 11. Oxidation behavior of UHTC at 1327°C in air.

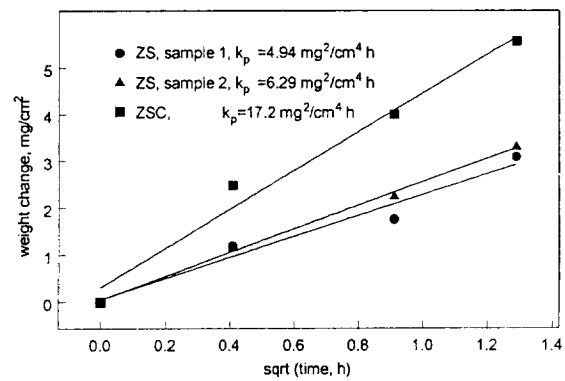


Figure 12. Parabolic oxidation behavior displayed by ZS and ZSC at 1327°C in air.

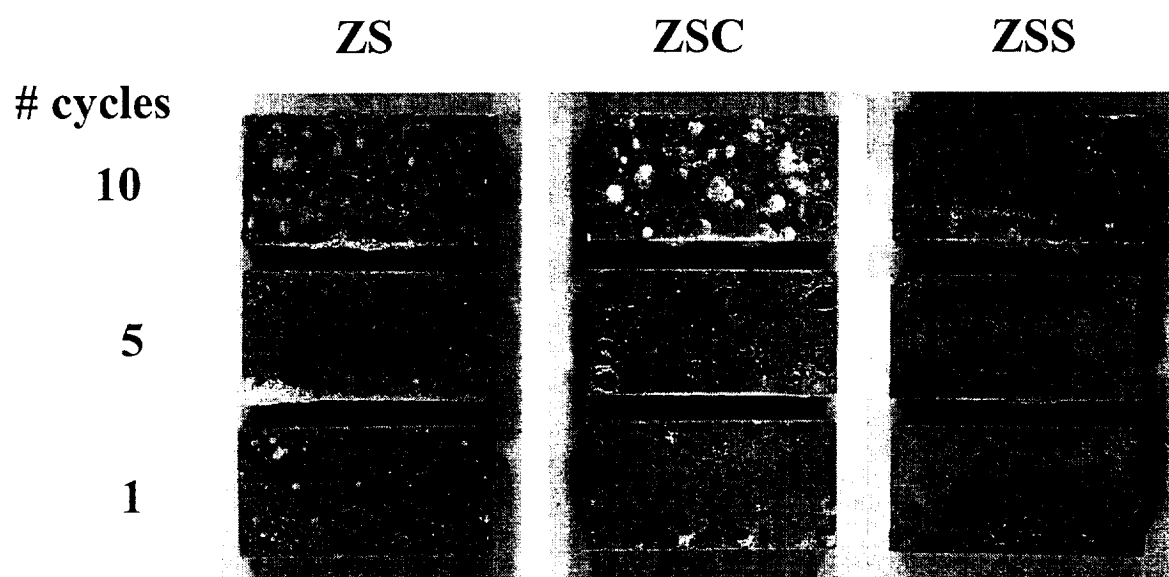


Figure 13. Comparison of UHTC oxidized in air at 1627°C for 10 minute cycles.

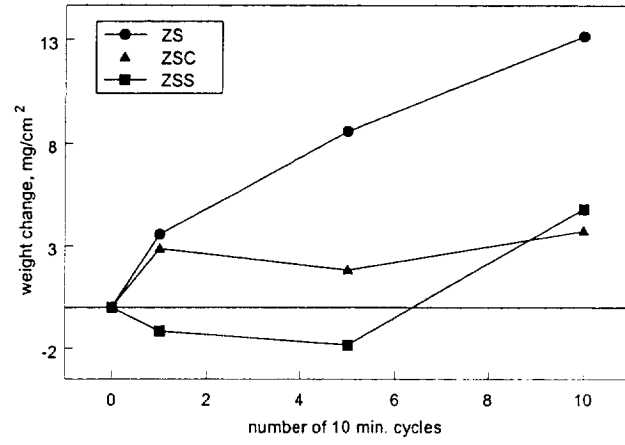


Figure 14. Oxidation behavior of UHTC at 1627°C in air.

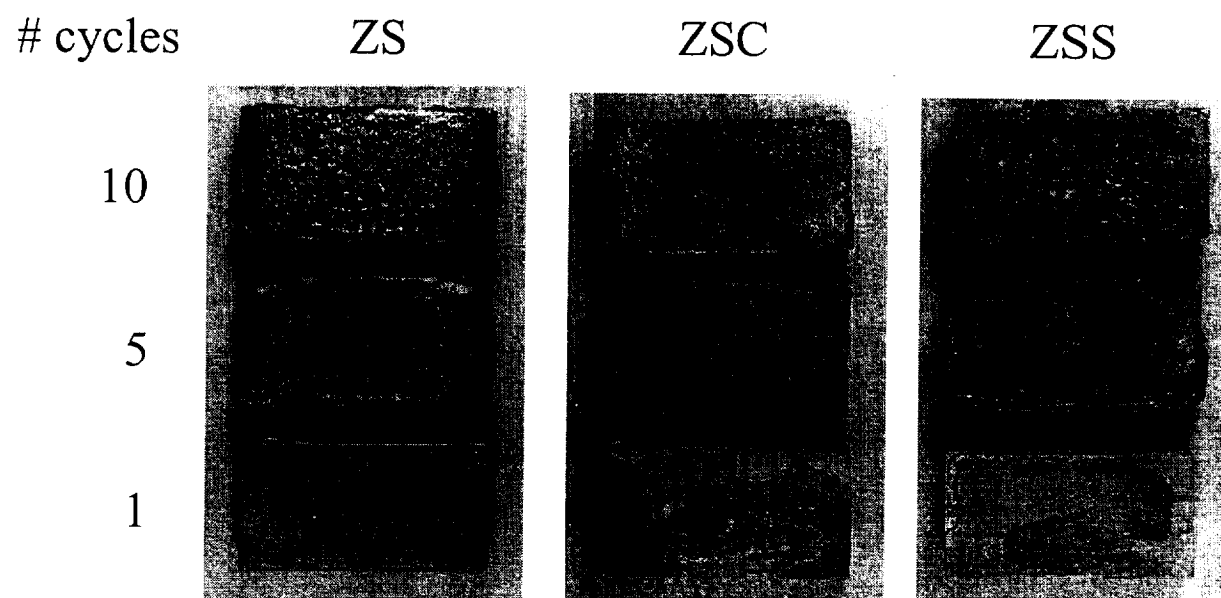


Figure 15. Comparison of the oxidation behavior of UHTC oxidized in air at 1927°C for 10 minute cycles.

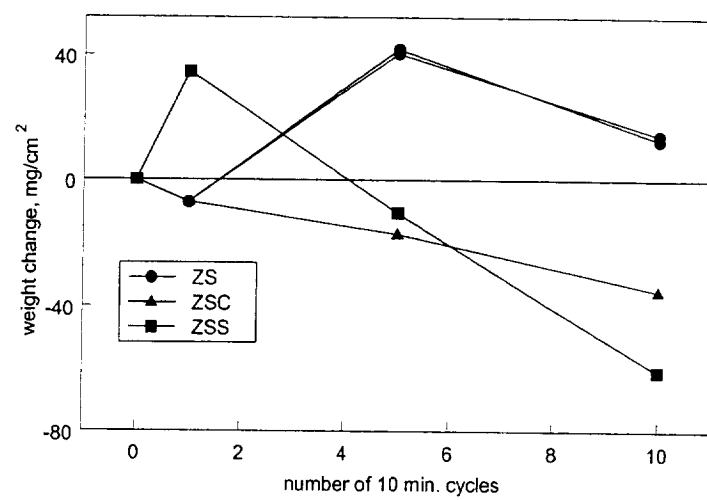


Figure 16. Oxidation behavior of UHTC at 1927°C in air.



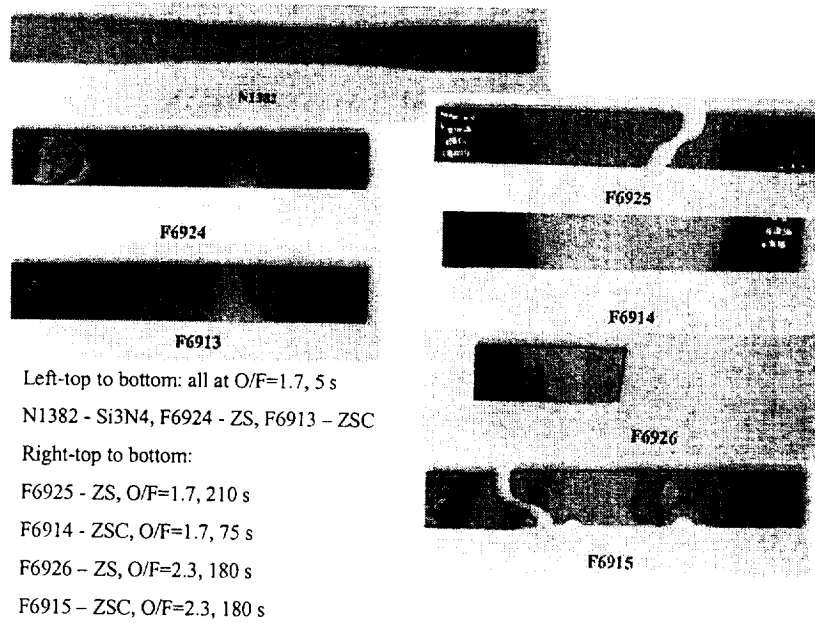


Figure 17. Photographs of specimens tested in thermal shock.